Beam-Target Helicity Asymmetry E in $K^0\Lambda$ and $K^0\Sigma^0$ Photoproduction on the Neutron

D. H. Ho,[1,*] R. A. Schumacher,[1,†] and A. D'Angelo, A. Deur, J. Fleming, C. Hanretty, T. Kageya, F. J. Klein, E. Klempt, M. M. Lowry, H. Lu, V. A. Nikonov, P. Peng, A. M. Sandorfi, A. V. Sarantsev, I. I. Strakovsky, N.K. Walford, X. Wei, R. L. Workman[2]

(The g14 Run Group, & CLAS Collaboration)

[1] *Department of Physics, Carnegie Mellon University, Pittsburgh, PA., 15213, USA*

[2] *Thomas Jefferson National Accelerator Facility, Newport News, VA, 23606, USA*

Helmholtz-Institute für Strahlen- und Kernphysik der Rheinischen Friedrich-Wilhelms Universität, Nussallee 14-16, 53115 Bonn, Germany

Particle and Nuclear Physics Institute, Orlova Rosha 1, 188300 Gatchina, Russia

(to be updated...)

(Dated: April 5, 2018)

We report the first measurements of the E beam-target helicity asymmetry for the $\vec{\gamma}\vec{n} \to K^0\Lambda$, and $K^0\Sigma^0$ channels in the energy range of 1.70$\leq W \leq$2.34 GeV. The CLAS system at Jefferson Lab used a circularly polarized photon beam and a target consisting of longitudinally polarized solid molecular hydrogen deuteride (HD) with low background contamination for the measurements. Comparisons with model predictions from the KaonMAID, SAID, and Bonn-Gatchina models are presented. These results will serve to help separate the isospin $I = 0$, and $I = 1$ photo-coupling transition amplitudes in pseudoscalar meson photoproduction.

I. INTRODUCTION

An accurate description of excited nucleons and their interaction with probes such as photons at GeV energies has remained elusive for decades. The Standard Model [1, 2] underpins the structure of the nucleons and their excitations, but in the low-energy non-perturbative regime competing semi-phenomenological models of specific reaction dynamics are necessary. Present-day lattice QCD calculations [3, 4] and quark models [5–10] predict a richer baryon spectrum than experimentally observed [11–13] —the so-called *missing resonance problem*. There are theoretical approaches for the nucleon resonance spectrum which predict that some quark-model states do not exist, including models with quasi-stable diquarks [14], AdS/QCD string-based models [15], and "molecular" models in which some baryon resonances are dynamically generated from the unitarized interaction among ground-state baryons and mesons [16]. But finding such missing states may in part be an experimental problem: high-mass nucleon resonances may couple only weakly to πN and may thus have escaped detection in the analysis of πN elastic scattering experiments. Further, they are wide and overlapping, and partial wave analysis of reaction data for specific final states remains difficult due to channel coupling effects and insufficient experimental constraints. The experimental results discussed here represent one step in the direction of adding constraints to the hyperon photoproduction database, which ultimately impacts models for nucleon excitations.

Cross section measurements alone are not enough to constrain PWA models of meson production amplitudes. Polarization observables related to the spins of the beam photons, target, and recoiling baryons are also needed. Photoproduction of pseudoscalar mesons is governed by four complex amplitudes that lead to an interaction cross sections and 15 spin observables [17]. To describe a *complete* experiment requires the measurement of a minimum of eight well-chosen observables [18–21] at any given center-of mass (c.m.) energy, W, and meson polar angle, $\cos\theta_{c.m.}$. Furthermore, while isospin I=3/2 transitions (Δ^* excitation) can be studied with proton target data alone, both proton- and neutron-target observ-

* current address ITG, Boston, MA

† contact: schumacher@cmu.edu

ables are necessary to study I=1/2 transitions and isolate the separate $\gamma p N^*$ proton and $\gamma n N^*$ neutron photocouplings [22]. Information from neutron targets is comparatively scarce [23], particularly in the hyperon channels [24, 25], which is why the present measurement is of value. Furthermore, the hyperon photoproduction channels $\gamma N \to K\Lambda(\Sigma^0)$ are attractive for analysis for two reasons. First, the threshold for two-body hyperon final states is at $W \simeq 1.6$ GeV, above which lie numerous poorly-known resonances. Two-body strange decay modes, rather than cascading non-strange many-body decays, may be easier to interpret. Second, the hyperons channels give easy access to recoil polarization observables on account of their self-analyzing weak decays. While the present measurement does not involve final-state polarizations, previous work has shown the benefit of using such information to extract properties of higher-mass nucleon resonances [26–33]. Thus, pursuing "complete" amplitude information in the hyperon photoproduction channels can be complimentary to the analogous quest in, say, pion photoproduction.

In this article, we present first-time measurements of the beam-target observable E on a longitudinally polarized neutron bound in deuterium in the quasi-free reaction $\gamma n(p) \to K^0 Y(p)$. The helicity asymmetry E is formally defined as the normalized difference in photoproduction yield between parallel (σ^P) and anti-parallel (σ^A) configurations, *i.e.*, settings where the incident photon beam polarization is aligned or anti-aligned, respectively, with the longitudinal polarization of the target. We write

$$E = \frac{\sigma^A - \sigma^P}{\sigma^A + \sigma^P}. \quad (1)$$

In terms of the cross section, this observable is defined as

$$\left(\frac{d\sigma}{d\Omega}\right) = \left(\frac{d\sigma}{d\Omega}\right)_0 (1 - P_T P_\odot E), \quad (2)$$

where $(d\sigma/d\Omega)_0$ is the differential cross section averaged over initial spin states and summed over final states, and P_T and $P_\odot$ are the target longitudinal and beam circular polarizations, respectively.

The asymmetry results obtained will be compared with several model predictions. The first is a single-channel effective Lagrangian approach, KaonMAID [34, 35], with parameter constraints largely from SU(6). Without experimental constraints on the $N^*\Lambda K^0$ and $\gamma n N^*$ vertices, the reaction of interest is difficult to model accurately. The second model giving predictions for the present results is the data description given by SAID [36, 37]. In general, SAID is more up to date than the KaonMAID model; for the present reaction channels the predictions are a polynomial fit to all available data from before about 2008, assuming final state interactions for these polarization observables can be neglected [38]. The third comparison is made to the multi-channel K-matrix formalism of the Bonn-Gatchina [39] group, which is most up to date, being constrained by recent first-time measurements [24] of the differential cross section for the reaction $\gamma n(p) \to K^0\Lambda(p)$ (with (p) as the spectator proton).

II. EXPERIMENTAL PROCEDURES

The experiment was performed at the Thomas Jefferson National Accelerator Facility (JLab) using the CEBAF Large Acceptance Spectrometer (CLAS) [40]. This setup has been used for several studies of K^+ photoproduction of hyperonic final states on a proton target [27–29, 31, 32, 41–43] and on an effective neutron (deuteron) target [24, 25]. The present results stem from the so-called "g14" run period between December 2011 and May 2012, from which non-strange results have been previously reported [44]. The CEBAF accelerator provided longitudinally polarized electron beams with energies of $E_e = 2.281$ GeV, 2.257 GeV, and 2.541 GeV, and an *average* electron beam polarization for the present study of $P_e = 0.82 \pm 0.04$, which was measured routinely by the Hall-B Möller polarimeter. The electron beam helicity was pseudo-randomly flipped between +1 and −1 with a 960 Hz flip rate. The electron beam was incident on the thin gold radiator of the Hall-B Tagger system [45] and produced circularly polarized tagged photons. The polarization of the photons was determined using the Maximon and Olsen formula [46]

$$P_\odot = P_e \frac{4k - k^2}{4 - 4k + 3k^2}, \quad (3)$$

where $P_\odot$ and P_e are the photon and electron polarizations, respectively, and $k = E_\gamma/E_e$ is the ratio between the photon energy and the electron beam energy.

A 5-cm-long solid target of hydrogen deuteride (HD) target was used in the experiment [47, 48]. It achieved polarizations of 25-30% for deuterons, i.e. for *bound* neutrons in the deuteron with relaxation times of about a year. The polarized target was held at the center of CLAS using an in-beam cryostat (IBC) that produced a 0.9 Tesla holding field and operated at 50 mK. The target polarization was monitored using nuclear magnetic resonance measurements [47]. The orientation of the target longitudinal polarization direction was flipped between periods of data taking, either parallel or anti-parallel to the direction of the incoming photon beam. Background events from the unpolarizable target wall material and aluminum cooling wires [48] were removed using empty-target data, as discussed in Sec. III A and III B.

The specific reaction channel for this discussion came from events of the type $\gamma d \to \pi^+\pi^-\pi^- p(X)$ using a read-out trigger requiring a minimum of two charged particles in different CLAS sectors. After particle identification we required the "spectator", X, to be an undetected low-momentum proton and possibly a photon, via the missing mass technique, as explained in the next section. In order to determine the E asymmetry experimentally, the event yields in a given kinematic bin of W and kaon center-of-mass angle were obtained by counting events with total c.m. helicity h =3/2 (lab frame anti-parallel configuration) called N_A and 1/2 (lab frame parallel configuration) called N_P, respectively. The E observable was then computed as

$$E = \frac{1}{\overline{P_T} \cdot \overline{P_\odot}} \left(\frac{N_A - N_P}{N_A + N_P} \right), \tag{4}$$

where $\overline{P_T}$ and $\overline{P_\odot}$ are the run-averaged target and beam polarizations, respectively.

III. DATA ANALYSIS

The performance of the system was extensively studied for a reaction with much higher count-rates than the present one. The non-strange reaction $\gamma d \to \pi^- p(X)$ was investigated using many of the same analysis steps and methods discussed in this article to extract the E observable for $\gamma n \to p\pi^-$ [44]. The analysis steps outlined below were all tested on that reaction. In particular, the Boosted Decision Tree (BDT) selection procedure used below was validated against alternative "cut-based" and kinematic fit methods, with the result that the BDT procedure resulted in $\sim 30\%$ larger yields of signal event and therefore gave better statistical precision on the final E asymmetry.

A. Particle identification

For this particular analysis, we required that every selected event consist of at least two positive tracks and two negative tracks with associated photon tagger hits [45]. The CLAS detector system determined the path length, the charge type, the momentum and the flight time for each track [49–51]. For each track of momentum $\overrightarrow{p}$, we compared the measured time of flight, TOF_m, to a hadron's expected time of flight, TOF_h, for a pion and proton of identical momentum and path length. CLAS-standard cuts were placed on the difference between the measured and expected time of flight, $\triangle TOF = TOF_m - TOF_h$. We selected events of which the two positively charged particles were the proton and π^+, and the two negatively charged were both the π^-. Well-established CLAS fiducial cuts were applied to select events with good spatial reconstruction.

Events originating from unpolarized target material—aluminum cooling wires, and polychlorotrifluoroethylene (pCTFE) dilute the measurement and must be taken into account. A period of data taking was dedicated to an *empty* target cell in which the frozen HD material was not present. This set of data was used to study and remove the bulk of the target material background on the basis of a loose missing mass cut. Figure 1 shows the resulting reconstructed reaction vertex for 4-track data along the beam line for both a full target and for an empty target scaled to match the counts in several downstream target foils. The full-to-empty ratio of about 3.3:1 in the target region was important in selecting the optimal BDT cut discussed below.

Figure 2 shows the resulting target-full missing mass distribution for spectator X in $\gamma d \to \pi^-\pi^+\pi^- p(X)$, after these cuts. A clear peak corresponding to the spectator proton is seen. Then we applied a loose cut to reject events with missing mass higher than 1.4 GeV/c^2 because of the presence of $\Sigma^0 \to \pi^- p(\gamma)$ events, which result in a

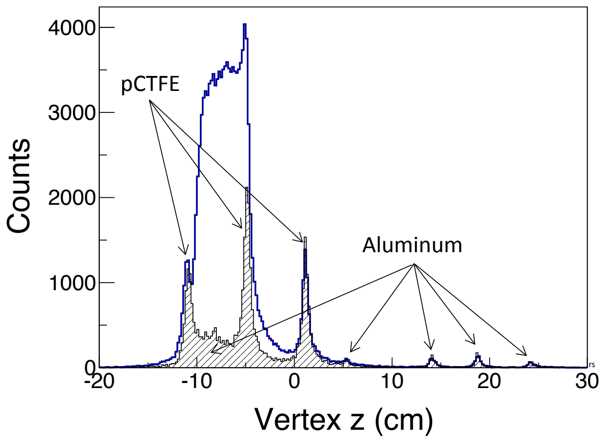

FIG. 1. The reconstructed distribution of the reaction vertex along the beam line for a full target as the open histogram. The peaks at $z > 0$ are from target-independent foils in the cryostat. The dark histogram is the target-empty measured background (BG), which consisted mostly of aluminum wires and foils, scaled to match the downstream foils.

tail on the high-mass side of the proton peak.

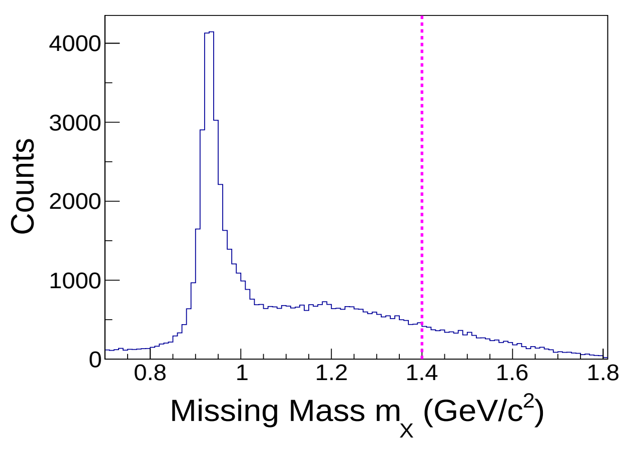

FIG. 2. The missing mass distribution, $\gamma d \to \pi^-\pi^+\pi^- pX$ after PID cuts showing the dominant spectator proton peak. The magenta line indicates a loose event rejection for $m_x >$ 1.4 GeV/c^2. This rejects unambiguous background but keeps $\Sigma^0 \to \pi^- p(\gamma)$ events in which both a proton and a photon are missing.

B. K^0Y event selection using BDT analysis

Because of the rather low statistics in this experiment, a method was needed to optimally isolate the events of interest with minimal statistics loss. The multivariate analysis tool called the Boosted Decision Tree (BDT) approach was used to select the exclusive events of interest in this study. Three steps were needed to achieve this result. The first BDT was created to select events from both the $\gamma d \to \pi^-\pi^+\pi^- p(p_S)$ and $\gamma d \to \pi^-\pi^+\pi^- p(p_S\gamma)$ final states, consistent with quasi-free production from a deuteron. This was to reject target-material background and events with high missing momentum of the undetected spectator nucleon, p_S. The second BDT was created to remove the non-strange pionic background with the same final states, that is, to pick out events with Λ and Σ^0 intermediate-state particles. The third BDT was to separate the $K^0\Lambda$, and $K^0\Sigma^0$ events.

This BDT algorithm is more efficient than a simple "cut" method in both rejecting background and keeping signal events [52]. The method builds a "forest" of *distinct decision trees* that are linked together by a *boosting* mechanism. Each decision tree constitutes a *disjunction* of logical conjunctions (i.e., a graphical representation of a set of *if-then-else* rules). Thus, the entire reaction phase-space is considered by every decision tree. Before employing the BDT for signal and background classification, the BDT algorithm needs to be constructed (or trained) with *training* data—of which the category of every event is definitively known. We used the ROOT implementation of the BDT algorithm [53]. Every event processed by the constructed BDT algorithm is assigned a value between -1 and $+1$ that quantifies how likely the processed event is a background event (closer to -1) or a signal event (closer to $+1$). An optimal cut on the BDT output is chosen to maximize the $S/\sqrt{S+B}$ ratio, where S, B are the estimations, based on training data, of the initial number of signal and background events, respectively.

The initial assignment of the π^- particles to either K^0 or Λ decay was studied with Monte Carlo simulation, and a loose selection based on invariant masses was made. Specific details of these cuts are found in Ref. [52].

The first BDT was trained using real empty-target data for the background training. A signal Monte-Carlo simulating quasi-free hyperon production on the neutron was used for signal training data. The momentum distribution of the spectator proton, p_s, followed the Hulthèn potential [54, 55] for the deuteron. Based on this training, an optimal BDT cut that maximized the estimated initial $S/\sqrt{S+B}$ ratio was selected. Figure 3 shows the total (blue histogram) and rejected (black histogram) events by the first BDT cut. Two things should be noted when comparing Figs. 1 and 3. Firstly, the BDT was trained to remove target-material background events with missing momentum not consistent with a Hulthèn distribution. Secondly, the BDT background-rejection efficiency was not perfect, leaving some target-material background events that was removed in a subsequent step (Sec. III C). We then rejected events with $z > -2$ cm on the reaction vertex to remove remaining unambiguous background events due to various cryostat foils.

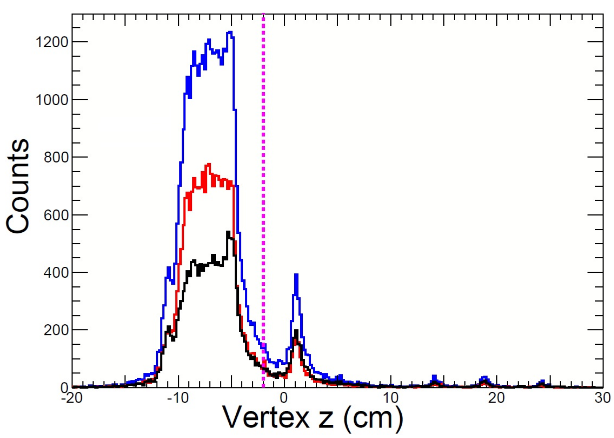

FIG. 3. The reconstructed distribution of the reaction vertex along the beam line showing target-full events in the top histogram (blue) after the loose K^0Y^0 selection and the missing mass cut shown in Fig. 2. Events selected by the first BDT are the middle histogram (red), and the rejected events are the bottom histogram (black). The magenta line indicates a loose cut to reject unambiguous target-material background.

The second-step BDT was trained using a 4-body phase-space $\gamma d \to \pi^-\pi^+\pi^- p(p_S)$ simulation as background training data and the $\gamma d \to K^0\Lambda(p_S)$ simulation as signal training data. There were two negative pions in each event: one from the decay of the K^0 and one from the decay of the hyperon. The goal of the BDT analysis was to use the available correlations among all particles to sort the pions correctly and to select events with decaying strange particles. The main training variables at this stage of the analysis included the 3-momenta of all the particles and the detached decay vertices of the K^0s and the hyperons. After the optimized BDT cut was placed, Fig. 4 shows the total (red histogram) and rejected (black histogram) events after this second BDT analysis step. The efficiency of the second BDT was less than 100%, thus, there are remaining target background events in the selected data sample. The dips near the signal maxima in the background spectra show that the background is slightly undersubtracted. We address this issue below. A simple fit with a Breit-Wigner line shape and a polynomial was used to estimate that the strange-to-non-strange ratio of events in the data set at this stage was about 2.3:1 in the peak regions.

For the final task, separating the $K^0\Lambda$, and $K^0\Sigma^0$ channels, the third BDT was trained using $\gamma d \to K^0\Sigma^0(p_S)$ simulation as "background" training data and $\gamma d \to K^0\Lambda(p_S)$ simulation as "signal" training data. Note that the term "background" used here is just for semantic convenience, since both channels were retained after applying the third optimized BDT cut. Figure 5 shows in the left (right) histogram the classification success of the third BDT on $\gamma d \to K^0\Lambda(p_S)$ ($\gamma d \to K^0\Sigma^0(p_S)$) simulation data. The histograms reveal that a small number of $K^0\Lambda$ events would be misclassified as $K^0\Sigma^0$ events and vice-versa. In the next section correction for the contamination on both final data sets will be discussed. Figure 6 shows the separation result from the third BDT on real data.

C. Corrections for remaining backgrounds and asymmetry calculation

The E asymmetry values for both target-material and non-strange background events were statistically consistent with zero [52]; therefore, we implemented an approximation procedure to correct for the dilution effect from the remaining background. We estimated two ratios: one for the remaining fraction of target background (TGT), R^{TGT}, and one for the fraction of remaining non-strange (NS) final-state events mixed with the hyperon events, R^{NS}. We write $R^{TGT} = \frac{N^{remain}}{N^{HD}}$, and

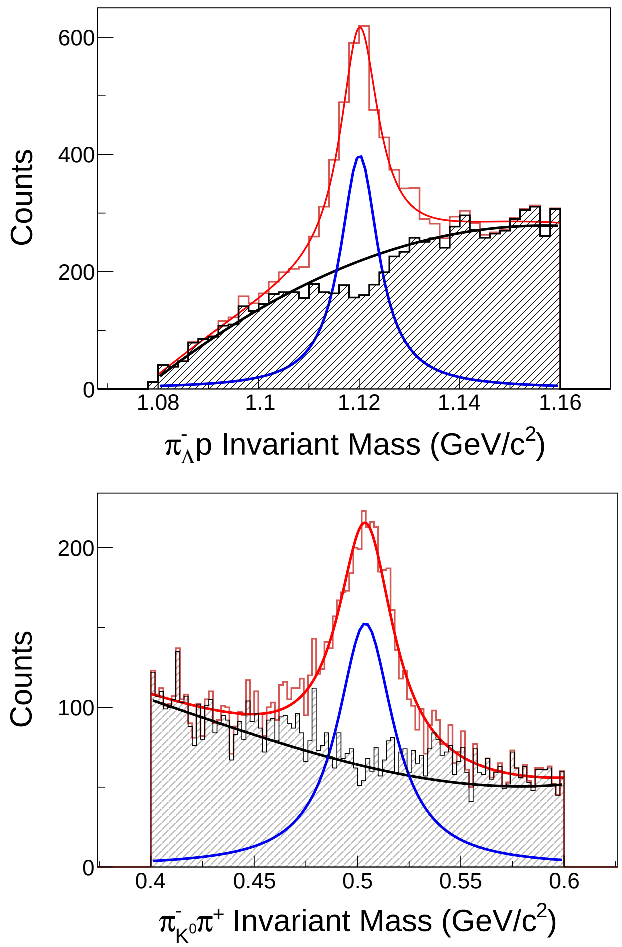

FIG. 4. The invariant $\pi^-_\Lambda p$ mass (top) and invariant $\pi^-_{K^0}\pi^+$ mass (bottom) after target material background rejection by the first BDT cut. The black histograms show events rejected events by the second BDT cut. A fit of a sum (red) of a Breit-Wigner line-shape (blue) and a 3^{rd} order polynomial (black) is shown.

$R^{NS} = \frac{Y^{remain}}{Y^{K^0Y}}$. N^{remain} and N^{HD} are the estimated number of remaining target-material background events and the true deuteron events after the first BDT and $z = -2$ cm vertex cuts, respectively. Y^{remain} and Y^{K^0Y} are the estimated number of remaining non-strange and true K^0Y events after the second BDT cut, respectively. Next, let Y_{BDT} be the number of events that passed the z-vertex cut and the first two BDT selections, then Y_{BDT} can be partitioned into

$$\begin{aligned} Y_{BDT} &= \left(1 + R^{NS}\right) Y^{K^0Y} \\ &= \left(1 + R^{NS}\right) \left[Y^{K^0Y}_{HD} + Y^{K^0Y}_{TGT}\right], \end{aligned} \tag{5}$$

since Y^{K^0Y} also comprises of events from the remaining target-material background and the bound signal events. If we further allow $\frac{Y^{K^0Y}_{TGT}}{Y^{K^0Y}_{HD}} = \frac{N^{remain}}{N^{HD}} = R^{TGT}$, then Y_{BDT} can finally be expressed as:

$$Y_{BDT} = \left(1 + R^{NS}\right)\left(1 + R^{TGT}\right) Y^{K^0Y}_{HD}, \tag{6}$$

or

$$Y^{K^0Y}_{HD} = \left(1 + R^{NS}\right)^{-1}\left(1 + R^{TGT}\right)^{-1} Y_{BDT}. \tag{7}$$

These relations should remain valid for both $Y^{K^0\Lambda}_{BDT}$ and $Y^{K^0\Sigma^0}_{BDT}$, which are the $K^0\Lambda$ and $K^0\Sigma^0$ signal events from neutrons bound in deuterium, respectively. The backgrounds that leak through the BDT filters will be helicity independent and will subtract in the numerator of the asymmetry of Eq. 4. Using Eq. 7 to correct the summed yields in the denominator gives the corrected asymmetry as

$$E^{K^0Y}_{corrected} = \left(1 + R^{NS}\right) \times \left(1 + R^{TGT}\right) E^{K^0Y}_{BDT}, \tag{8}$$

where $E^{K^0Y}_{BDT}$ is obtained from $Y^{K^0Y}_{BDT}$ (or, more exactly, Y^P_{BDT} and Y^A_{BDT} of the K^0Y parallel and anti-parallel subsets). From the simulations we found average values of R^{TGT} and R^{NS} of 0.09 and 0.17, respectively, with some dependence on the specific run period.

Next we discuss a correction for the third BDT classification result. Recall that the third BDT selection separates the true signal K^0Y events into two subsets: one is mostly $K^0\Lambda$ events, and the other is mostly $K^0\Sigma^0$. If we denote N^{BDT}_Λ and $N^{BDT}_{\Sigma^0}$ as the number of events the third BDT identified as $K^0\Lambda$ and $K^0\Sigma^0$ events, respectively, then we have the expressions

$$N^{BDT}_\Lambda = \omega_\Lambda N^{true}_\Lambda + (1 - \omega_{\Sigma^0}) N^{true}_{\Sigma^0}, \tag{9}$$

$$N^{BDT}_{\Sigma^0} = (1 - \omega_\Lambda) N^{true}_\Lambda + \omega_{\Sigma^0} N^{true}_{\Sigma^0}, \tag{10}$$

where ω_Λ and ω_{Σ^0} are the fractions of events correctly identified—these values were estimated based on simulation data. After rearrangement, we arrive at the expressions

$$\begin{aligned} N^{true}_\Lambda = &\left[\omega_\Lambda - \frac{(1 - \omega_{\Sigma^0})}{\omega_{\Sigma^0}}(1 - \omega_\Lambda)\right]^{-1} \\ &\times \left[N^{BDT}_\Lambda - \frac{(1 - \omega_{\Sigma^0})}{\omega_{\Sigma^0}} N^{BDT}_{\Sigma^0}\right], \end{aligned} \tag{11}$$

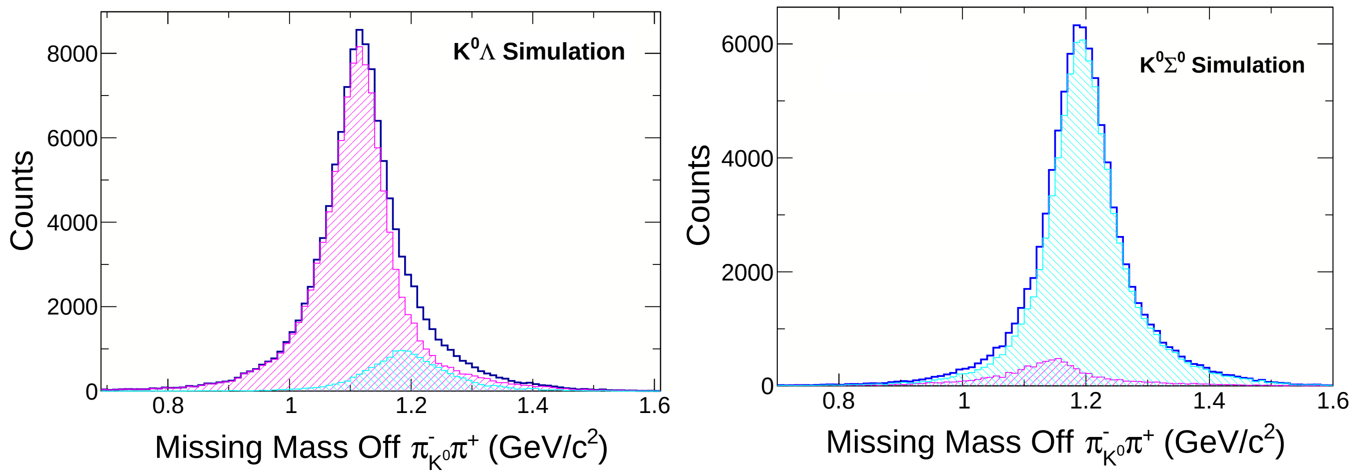

FIG. 5. The distribution of missing mass off the reconstructed K^0, $\gamma n \to \pi^-_{K^0}\pi^+ X$ for simulation data, assuming that the target is an at-rest neutron. On the left, the magenta histogram represents events with correct $K^0\Lambda$ classification, while the cyan histogram represents events with *wrong* $K^0\Sigma^0$classification. On the right, the cyan histogram represents events with correct $K^0\Sigma^0$ classification, while the magenta histogram represents events with the *wrong* $K^0\Lambda$ classification.

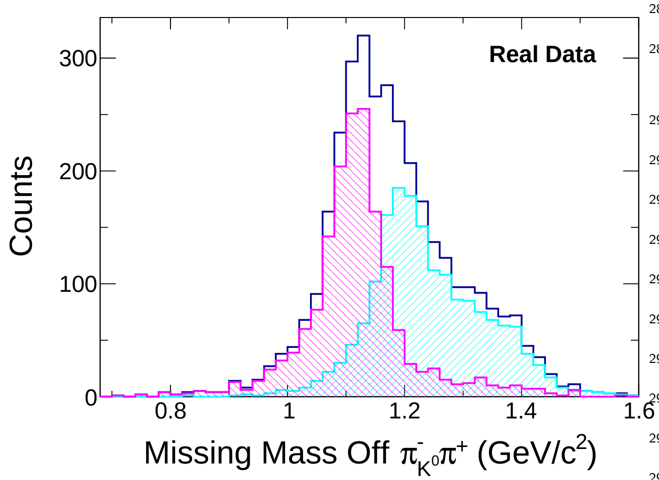

FIG. 6. The distribution of missing mass off the reconstructed K^0, $\gamma n \to \pi^-_{K^0}\pi^+ X$ for real data, assuming that the target is an at-rest neutron, after rejecting non-hyperon background by the second BDT cut. The magenta (cyan) histogram was classified as $K^0\Lambda$ ($K^0\Sigma^0$) using the third BDT selection step.

$$N^{true}_{\Sigma^0} = \left[\omega_{\Sigma^0} - \frac{(1-\omega_\Lambda)}{\omega_\Lambda}(1-\omega_{\Sigma^0})\right]^{-1} \times \left[N^{BDT}_{\Sigma^0} - \frac{(1-\omega_\Lambda)}{\omega_\Lambda}N^{BDT}_\Lambda\right] . \quad (12)$$

The *corrected* E asymmetry was obtained using the derived N^{true}_Λ and $N^{true}_{\Sigma^0}$ by using Eq. 4. From the simulations we found average values of ω_Y of 0.87 and 0.91 for Λ and Σ^0 events, respectively.

The neutron polarization in the deuteron is smaller than the deuteron polarization because the deuteron wavefunction has, in addition to an S-wave component, a D-wave component in which the spin of the neutron need not be aligned to the deuteron spin. This was studied using data for $\gamma n \to \pi^- p$ reaction and reported in our previous publication Ref. [44]. It was found that for a spectator recoil momenta of less than 100 MeV/c the correction was negligible. Had we cut on recoil momentum at 200 MeV/c rather than 100 MeV/c, a measured dilution factor of $(8.6 \pm 0.1)\%$ would have been necessary for the non-strange channel. But different reaction channels may exhibit different sensitivities to recoil momentum. For the reaction under discussion here we could not afford the statistical loss by cutting on recoil momentum, and we elected to make a conservative correction based on the general considerations of Ref. [56]. The neutron polarization can be estimated as $P_n = P_d(1-\frac{3}{2}P_D)$, where P_n and P_d are neutron and deuteron polarizations, respectively, and P_D denotes the deuteron D-state probability. The latter is not strictly an observable and need only be treated consistently within a given NN potential. Following this paper, we take the D-state contribution averaged over a range of NN potentials as about 5%, which implies the neutron polarization is 92.5% of the deuteron polarization, or a 7.5% dilution factor.

D. Systematic Uncertainties

We implemented four systematic studies to quantify the robustness of the trained BDT algorithms and the sensitivity of our result on the correction procedures introduced in the previous section. Two tests studied the effect of loosening the first and the second BDT cuts, respectively. One test focused on the sensitivity of the E results on the third correction — the correction procedure that was implemented to "purify" the final selected $K^0\Sigma^0(K^0\Lambda)$ sample. Lastly we reduced the beam and target polarizations by one standard deviation of their respective total uncertainties (statistical and systematic) to study the changes on the E results. As will be seen in the tabulated results of Table I , however, the dominating uncertainties are always statistical.

IV. RESULTS

We present here the result for the E asymmetry in two W energy bins. The lower W energy bin is from 1.70 GeV to 2.02 GeV and denoted as W_1, while the higher W energy bin is from 2.02 GeV to 2.34 GeV and referred to as W_2. Due to small cross sections for K^0Y photoproduction, and to detector inefficiencies that are amplified by the required identification of four charged particles, out statistics are sufficient for only three bins in K^0 center-of-mass production angle. The measurements for the $\gamma n \to K^0\Lambda$ reaction are plotted together with predictions from the KaonMAID, SAID, and Bonn-Gatchina (BnGa) models in Fig. 7. The data show that the $K^0\Lambda$ asymmetry is largely positive below 2 GeV and mostly negative above 2 GeV, without more discernible trends. Values of E must approach +1 at $\cos\theta^{c.m.}_{K^0} \to \pm 1$ to conserve angular momentum. Thus, the values for E in bin W_2 must change rather rapidly near the extreme angles.

None of the models were tuned to these results; that is, the models are all predictions based on fits to previously published data on other observables. First, one observes that the data are not statistically strong enough to strongly discriminate among the models. In the lower W bin all three models can be said to agree with the data. In the higher W bin the SAID model may be slightly favored by the data among the three.

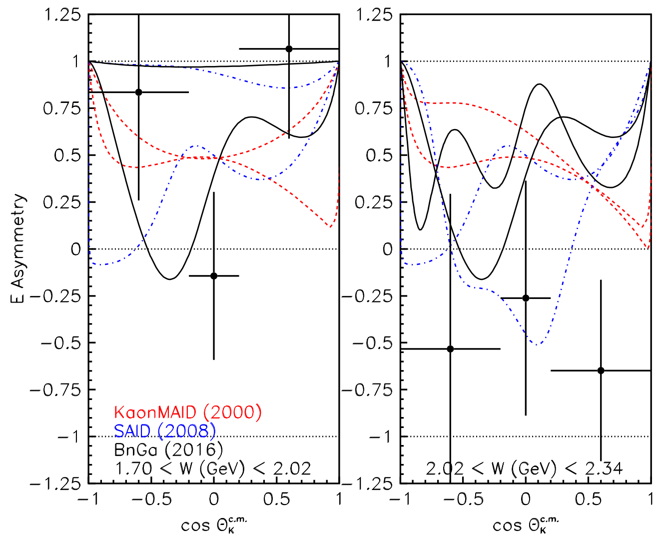

FIG. 7. The helicity asymmetry E for the $K^0\Lambda$ final state (with combined statistical and systematic uncertainties) vs. $\cos\theta_{K^0}$ for two 0.32 GeV-wide energy bands in W, as shown. The asymmetries are shown with the neutron-target theoretical models KaonMaid [34] (red dashed), and SAID [36] (blue dot-dashed) and Bonn-Gatchina [30, 39] (solid black). Because of the very wide W bins, each model is represented by two curves, computed at the bin endpoint W values.

The results for the $\gamma n \to K^0\Sigma^0$ channel are plotted in Fig. 8, together with model predictions from SAID and Kaon-MAID. In contrast to the $K^0\Lambda$ channel at lower W, here the data hint at less positive values for E. In the bin for W above 2 GeV, the data are also consistent with zero for $K^0\Sigma^0$, whereas the $K^0\Lambda$ data tended to be negative. In fact, the $K^0\Sigma^0$ asymmetry is consistent with zero in all available bins. The model comparisons show that the the KaonMAID prediction for the $K^0\Sigma^0$ channel in the higher W bin are probably not consistent with the data, while the SAID result is consistent with the data. For the $K^0\Sigma^0$ case we do not have predictions from the Bonn-Gatchina model for the following reason: the unpolarized differential cross section has not been measured yet, and without it the model does not have a prediction available.

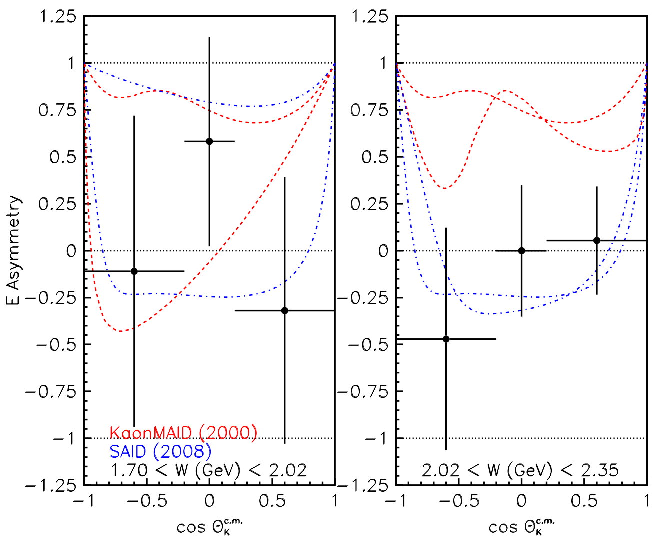

FIG. 8. The helicity asymmetry E for the $K^0\Sigma^0$ final state (with combined statistical and systematic uncertainties) vs. $\cos\theta_{K^0}$ for two 0.32 GeV-wide energy bands in W, as shown. The model curves are as for the previous figure.

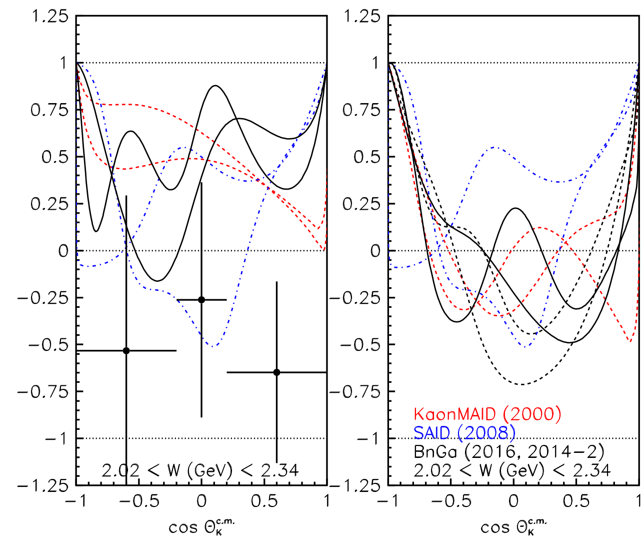

FIG. 9. The helicity asymmetry E for the $K\Lambda$ final state vs. $\cos\theta_{K^0}$ for energy band W_2. On the left are the data from Fig. 7 together with model predictions for a NEUTRON target. On the right are model calculations for the $K^+\Lambda$ reaction on a PROTON target, as computed using Kaon-Maid [34] (red dashed), SAID [36] (blue dot-dashed) and Bonn-Gatchina [30, 39] (black and black-dashed). The curves on the right are closer to the (reaction mismatched) data shown on the left.

In order to show one other comparison between data and theory, we plot some of the present results for a neutron target together with the model predictions for the $K^+\Lambda$ reaction on a *proton* target in Fig. 9. This is intended to show the difference between the model predictions on the proton and the neutron. One sees how different the three model predictions are for protons versus neutrons. One notes that the predictions for the proton target calculations all tend to be closer to the new data we are presenting for a neutron target. This suggests that calculations of the E observable for a neutron target can be improved. Thus, we may expect these present results to have some impact on the further development of these models.

So-far unpublished CLAS results for the corresponding reaction $\gamma p \to K^+\Lambda$ have higher statistics and finer energy bins than the present results (since the identification of this finals state requires the detection of fewer particles). The present $K^0\Lambda$ results are, within our errors, similar to the $K^+\Lambda$ asymmetries in Ref. [57].

The numerical values of the measured E asymmetries and their statistical and systematic uncertainties are reported in Table I. Note that the statistical uncertainties are larger than the systematic uncertainties.

V. CONCLUSIONS

We have reported the first set of the E asymmetry measurements for the reaction $\gamma d \to K^0 Y(p_s)$ for 1.70 GeV$\leq$ W $\leq$ 2.34 GeV. In particular, we described the three-step BDT-based analysis method developed to select a clean sample of $p\pi^+\pi^-\pi^-$ with intermediate hyperons. We have plotted the E asymmetry as a function of $\cos\theta^{CM}_{K^0}$. Several systematic uncertainty tests led to the conclusion that statistical uncertainties dominated the final results. The numerical values of the measured E asymmetries and their statistical and systematic uncertainties are reported in Table I.

Evidently, this analysis is limited by low statistics for the channels of interest, leading to large uncertainties on the measurements of the E asymmetry. At present, comparison with several models makes no decisive selections among the model approaches. The BnGa predictions are perhaps better than the SAID predictions,

		$\cos\theta_{K^0}$		
		−0.6	0.0	+0.6
$K^0\Lambda$	W_1	0.834±0.499±0.287	−0.144±0.436±0.098	1.066±0.419±0.231
	W_2	−0.533±0.752±0.345	−0.263±0.618±0.101	−0.648±0.464±0.136
$K^0\Sigma^0$	W_1	−0.110±0.723±0.406	0.581±0.539±0.144	−0.319±0.541±0.460
	W_2	−0.471±0.446±0.391	0.0002±0.317±0.150	0.054±0.281±0.065

TABLE I. Numerical values of the E asymmetry measurements for $K^0\Lambda/K^0\Sigma^0$ channels. The uncertainties are statistical and systematic, respectively. The center-of-mass energy ranges are $1.70 < W_1 < 2.02$ GeV and $2.02 < W_2 < 2.34$ GeV.

which in turn tend to be more favored than the Kaon-MAID predictions for both hyperon channels. Among all three model comparisons, the distinction between proton and neutron target predictions are differentiated by the data: The proton-target predictions compare better than the neutron-target predictions with the experimental results. In principle, this information is valuable since it hints at the necessary isospin decomposition of the hyperon photoproduction mechanism.

At present, multipole analyses for the K^0Y channels are severely limited by available data. Higher statistics data on these channels for a number of other polarization observable, from a much longer (unpolarized) target, has been collected during the $g13$ running period with CLAS and is under analysis. A greater number of different polarization observables is generally more effective than precision at determining a photoproduction amplitude [21]. When these $g13$ results become available, the present data on the beam-target E asymmetry are likely to have a larger impact.

ACKNOWLEDGMENTS

We acknowledge the outstanding efforts of the staff of the Accelerator and Physics Divisions at Jefferson Lab that made this experiment possible. The work of the Quark Interactions group at Carnegie Mellon University was supported by DOE grant DE-FG02-87ER40315. The Southeastern Universities Research Association (SURA) operated the Thomas Jefferson National Accelerator Facility for the United States Department of Energy under contract DE-AC05-06OR23177. Further support was provided by the National Science Foundation, the United Kingdom's Science and Technology Facilities Council grant ST/J000175, and the Italian Istituto Nazionale di Fisica Nucleare.

[1] David J. Gross and Frank Wilczek, "Ultraviolet Behavior of Nonabelian Gauge Theories," Phys. Rev. Lett. **30**, 1343–1346 (1973).

[2] H. David Politzer, "Reliable Perturbative Results for Strong Interactions?" Phys. Rev. Lett. **30**, 1346–1349 (1973).

[3] Robert G. Edwards, Jozef J. Dudek, David G. Richards, and Stephen J. Wallace, "Excited state baryon spectroscopy from lattice QCD," Phys. Rev. **D84**, 074508 (2011).

[4] R. G. Edwards, N. Mathur, D. G. Richards, and S. J. Wallace (Hadron Spectrum), "Flavor structure of the excited baryon spectra from lattice QCD," Phys. Rev. **D87**, 054506 (2013).

[5] Simon Capstick and W. Roberts, "Quark models of baryon masses and decays," Prog.Part.Nucl.Phys. **45**, S241–S331 (2000).

[6] Simon Capstick and W. Roberts, "Strange decays of nonstrange baryons," Phys. Rev. **D58**, 074011 (1998).

[7] Simon Capstick and Nathan Isgur, "Baryons in a Relativized Quark Model with Chromodynamics," *Proceedings, International Conference on Hadron Spectroscopy: College Park, Maryland, April 20-22, 1985*, Phys. Rev. **D34**, 2809 (1986), [AIP Conf. Proc.132,267(1985)].

[8] Ulrich Loring, Bernard C. Metsch, and Herbert R. Petry, "The Light baryon spectrum in a relativistic quark model with instanton induced quark forces: The Nonstrange baryon spectrum and ground states," Eur. Phys. J. **A10**, 395–446 (2001).

[9] L. Ya. Glozman, Willibald Plessas, K. Varga, and R. F.

Wagenbrunn, “Unified description of light and strange baryon spectra,” Phys. Rev. **D58**, 094030 (1998).

[10] M. M. Giannini, E. Santopinto, and A. Vassallo, “Hypercentral constituent quark model and isospin dependence,” Eur. Phys. J. **A12**, 447–452 (2001).

[11] C. Patrignani *et al.* (Particle Data Group), “Review of Particle Physics,” Chin. Phys. **C40**, 100001 (2016).

[12] Eberhard Klempt and Jean-Marc Richard, “Baryon spectroscopy,” Rev. Mod. Phys. **82**, 1095–1153 (2010).

[13] Roman Koniuk and Nathan Isgur, “Where Have All the Resonances Gone? An Analysis of Baryon Couplings in a Quark Model With Chromodynamics,” *Baryon 1980:217*, Phys. Rev. Lett. **44**, 845 (1980).

[14] Mauro Anselmino, Enrico Predazzi, Svante Ekelin, Sverker Fredriksson, and D. B. Lichtenberg, “Diquarks,” Rev. Mod. Phys. **65**, 1199–1234 (1993).

[15] Stanley J. Brodsky, “Hadron Spectroscopy and Structure from AdS/CFT,” Eur. Phys. J. **A31**, 638–644 (2007).

[16] E. E. Kolomeitsev and M. F. M. Lutz, “On baryon resonances and chiral symmetry,” Phys. Lett. **B585**, 243–252 (2004).

[17] I. S. Barker, A. Donnachie, and J. K. Storrow, “Complete Experiments in Pseudoscalar Photoproduction,” Nucl. Phys. **B95**, 347–356 (1975).

[18] C. G. Fasano, Frank Tabakin, and Bijan Saghai, “Spin observables at threshold for meson photoproduction,” Phys. Rev. **C46**, 2430–2455 (1992).

[19] Wen-Tai Chiang and Frank Tabakin, “Completeness rules for spin observables in pseudoscalar meson photoproduction,” Phys. Rev. **C55**, 2054–2066 (1997).

[20] Greg Keaton and Ron Workman, “Ambiguities in the partial wave analysis of pseudoscalar meson photoproduction,” Phys. Rev. **C54**, 1437–1440 (1996).

[21] A. M. Sandorfi, S. Hoblit, H. Kamano, and T. S. H. Lee, “Determining pseudoscalar meson photo-production amplitudes from complete experiments,” J. Phys. **G38**, 053001 (2011).

[22] A. M. Sandorfi and S. Hoblit, “Hyperon photoproduction from polarized H and D towards a *complete* N* experiment,” *Proceedings, 11th International Conference on Hypernuclear and Strange Particle Physics (HYP 2012): Barcelona, Spain, October 1-5, 2012*, Nucl. Phys. **A914**, 538–542 (2013).

[23] A. V. Anisovich, V. Burkert, N. Compton, K. Hicks, F. J. Klein, E. Klempt, V. A. Nikonov, A. M. Sandorfi, A. V. Sarantsev, and U. Thoma, “Neutron helicity amplitudes,” Phys. Rev. **C96**, 055202 (2017).

[24] N. Compton *et al.* (CLAS Collaboration), “Measurement of the differential and total cross sections of the $\gamma d \to K^0\Lambda(p)$ reaction within the resonance region,” Phys. Rev. C **96**, 065201 (2017).

[25] S. Anefalos Pereira *et al.* (CLAS), “Differential cross section of $\gamma n \to K^+\Sigma^-$ on bound neutrons with incident photons from 1.1 to 3.6 GeV,” Phys. Lett. **B688**, 289–293 (2010).

[26] C. A. Paterson *et al.* (CLAS), “Photoproduction of Λ and Σ^0 hyperons using linearly polarized photons,” Phys. Rev. **C93**, 065201 (2016).

[27] R. Bradford *et al.* (CLAS), “First measurement of beam-recoil observables C_x and C_z in hyperon photoproduction,” Phys. Rev. **C75**, 035205 (2007).

[28] R. Bradford *et al.* (CLAS), “Differential cross sections for $\gamma + p \to K^+ + Y$ for Λ and Σ^0 hyperons,” Phys. Rev. **C73**, 035202 (2006).

[29] J. W. C. McNabb *et al.* (CLAS), “Hyperon photoproduction in the nucleon resonance region,” Phys. Rev. **C69**, 042201 (2004).

[30] A. V. Anisovich, V. Kleber, E. Klempt, V. A. Nikonov, A. V. Sarantsev, and U. Thoma, “Baryon resonances and polarization transfer in hyperon photoproduction,” Eur. Phys. J. **A34**, 243–254 (2007).

[31] M. E. McCracken *et al.* (CLAS), “Differential cross section and recoil polarization measurements for the $\gamma p \to K^+\Lambda$ reaction using CLAS at Jefferson Lab,” Phys. Rev. **C81**, 025201 (2010).

[32] B. Dey *et al.* (CLAS), “Differential cross sections and recoil polarizations for the reaction $\gamma p \to K^+\Sigma^0$,” Phys. Rev. **C82**, 025202 (2010).

[33] A. V. Anisovich *et al.*, “N^* resonances from $K\Lambda$ amplitudes in sliced bins in energy,” Eur. Phys. J. **A53**, 242 (2017).

[34] T. Mart and C. Bennhold, “Evidence for a missing nucleon resonance in kaon photoproduction,” Phys. Rev. **C61**, 012201 (2000).

[35] F. X. Lee, T. Mart, C. Bennhold, and L. E. Wright, “Quasifree kaon photoproduction on nuclei,” Nucl. Phys. **A695**, 237–272 (2001).

[36] R. Arndt, W. Briscoe, I. Strakovsky, and R. Workman (George Washington Data Analysis Center), “SAID,” (2015), SAID web site `http://gwdac.phys.gwu.edu`.

[37] R. A. Adelseck, C. Bennhold, and L. E. Wright, “Kaon Photoproduction Operator for Use in Nuclear Physics,” Phys. Rev. **C32**, 1681–1692 (1985).

[38] I. Strakovsky (George Washington Data Analysis Center), “SAID,” (2017), Private Communication.

[39] A. V. Anisovich, R. Beck, E. Klempt, V. A. Nikonov, A. V. Sarantsev, and U. Thoma, “Pion- and photo-induced transition amplitudes to ΛK, ΣK, and $N\eta$,”

Eur. Phys. J. **A48**, 88 (2012).

[40] B. A. Mecking *et al.* (CLAS), "The CEBAF Large Acceptance Spectrometer (CLAS)," Nucl. Instrum. Meth. **A503**, 513–553 (2003).

[41] K. Moriya *et al.* (CLAS), "Spin and parity measurement of the $\Lambda(1405)$ baryon," Phys. Rev. Lett. **112**, 082004 (2014).

[42] K. Moriya *et al.* (CLAS), "Differential Photoproduction Cross Sections of the $\Sigma^0(1385)$, $\Lambda(1405)$, and $\Lambda(1520)$," Phys. Rev. **C88**, 045201 (2013), [Addendum: Phys. Rev.C88,no.4,049902(2013)].

[43] K. Moriya *et al.* (CLAS), "Measurement of the $\Sigma\pi$ photoproduction line shapes near the $\Lambda(1405)$," Phys. Rev. **C87**, 035206 (2013).

[44] D. Ho *et al.* (CLAS), "Beam-Target Helicity Asymmetry for $\vec{\gamma}\vec{n} \to \pi^- p$ in the N^* Resonance Region," Phys. Rev. Lett. **118**, 242002 (2017).

[45] D. I. Sober *et al.*, "The bremsstrahlung tagged photon beam in Hall B at JLab," Nucl. Instrum. Meth. **A440**, 263–284 (2000).

[46] Haakon Olsen and L. C. Maximon, "Photon and Electron Polarization in High-Energy Bremsstrahlung and Pair Production with Screening," Phys. Rev. **114**, 887–904 (1959).

[47] M. M. Lowry *et al.*, "A cryostat to hold frozen-spin polarized HD targets in CLAS: HDice-II," Nucl. Instrum. Meth. **A815**, 31–41 (2016).

[48] C. D. Bass *et al.*, "A portable cryostat for the cold transfer of polarized solid HD targets: HDice-I," Nucl. Instrum. Meth. **A737**, 107–116 (2014).

[49] Y. G. Sharabian *et al.*, "A new highly segmented start counter for the CLAS detector," Nucl. Instrum. Meth. **A556**, 246–258 (2006).

[50] M. D. Mestayer *et al.*, "The CLAS drift chamber system," Nucl. Instrum. Meth. **A449**, 81–111 (2000).

[51] E. S. Smith *et al.*, "The time-of-flight system for CLAS," Nucl. Instrum. Meth. **A432**, 265–298 (1999).

[52] Dao Ho, "Measurement of the E Polarization Observable for $\gamma d \to \pi^- p(p_s)$, $\gamma d \to K^0\Lambda(p_s)$, and $\gamma d \to \pi^+\pi^- d(0)$ using CLAS g14 Data at Jefferson Lab," Ph.D. Thesis, Carnegie Mellon University (2015), available online at `http://www.jlab.org/Hall-B/general/clas_thesis.html`.

[53] Andreas Hocker, Peter Speckmayer, Jorg Stelzer, Fredrik Tegenfeldt, and Helge Voss, "TMVA, toolkit for multivariate data analysis with ROOT," in *Statistical issues for LHC physics. Proceedings, Workshop, PHYSTAT-LHC, Geneva, Switzerland, June 27-29, 2007* (2007) pp. 184–187.

[54] J. B. Cladis, W. N. Hess, and B. J. Moyer, "Nucleon momentum distributions in deuterium and carbon inferred from proton scattering," Phys. Rev. **87**, 425–433 (1952).

[55] L. Lamia, M. La Cognata, C. Spitaleri, B. Irgaziev, and R. G. Pizzone, "Influence of the d-state component of the deuteron wave function on the application of the Trojan horse method," Phys. Rev. **C85**, 025805 (2012).

[56] G. Ramachandran, R. S. Keshavamurthy, and M. V. N. Murthy, "Target Asymmetry And Effective Neutron Polarization With Polarized Deuteron Targets," Phys. Lett. **87B**, 252–256 (1979).

[57] L. Casey, "The Search for Missing Resonances in $\gamma p \to K^+\Lambda$ Using Circularly Polarized Photons on a Longitudinally Polarized Frozen Spin Target," Ph.D. Thesis, Catholic University of America (2011), available online at `http://www.jlab.org/Hall-B/general/clas_thesis.html`.